Supplementary Information

Highly flexible yet strain-insensitive conjugated polymer

Wen Wen Deng,[a] Ze Ping Zhang,*[a] Min Zhi Rong*[a] and Ming Qiu Zhang*[a, b]

[a]Key Laboratory for Polymeric Composite and Functional Materials of Ministry of Education, GD HPPC Lab, School of Chemistry, Sun Yat-sen University, Guangzhou 510275, China

[b]Jieyang Branch of Chemistry and Chemical Engineering Guangdong Laboratory, Jieyang 515200, China

1. Experimental Section

1.1 Characterization

Proton nuclear magnetic resonance (^{1}H NMR) spectra were measured by using AVANCE III 400 MHz (400 MHz) spectrometer with dimethyl sulfoxide-d_6 (DMSO-d_6) as the solvent. All ^{13}C cross polarization/magic angle spinning (^{13}C CP/MAS) solid-state NMR experiments were performed on dry powder samples at ambient temperature. The number of scans in the ^{13}C CP/MAS experiments was 10000.

Fourier transform infrared (FTIR) spectra were recorded with Thermo Nicolet iS50 (USA) spectrometer. The micro-infrared spectroscopic analysis was performed on the same instrument using the continuum FTIR microscope attachment. The samples were coated onto a piece of 20 μm thick mirror aluminum plate and the FTIR spectra were collected on a square rectangle of 400 μm × 400 μm.

Matrix-assisted laser desorption ionization time-of-flight mass spectrometry (MALDI-TOF-MS) spectra were measured with UltrafleXtreme (Bruker Daltonics), which was equipped with a Nd:YAG laser and a collision cell. The measurement was operated with positive reflectron mode in the m/z range of 200–5000, and 2,5-dihydroxybenzoic acid (DHB) was used as the matrix.

Differential scanning calorimetry (DSC) tests were carried out on PerkinElmer DSC 4000 between -60 and 100 ºC at a heating rate of 10 ºC min^{-1} under N_2.

Dynamic mechanical analysis (DMA) was conducted on TA-DMA850 using tension mode with a strain of 0.5% at a heating rate of 3 ºC min^{-1} and frequency of 1 Hz. The molecular weight between crosslinks, M_c, was estimated using the following equation[1]:

$$M_c = \frac{3\rho RT}{E''} \qquad (1)$$

where T denotes the absolute temperature, R gas constant, ρ density, and E'' loss modulus, respectively.

Ultraviolet-visible-near-infrared (UV-vis-NIR) spectra were collected using a Perkin Elmer Lambda 950 spectrometer.

Raman spectra were recorded with a Thermo Fisher DXR3xi (USA) spectrometer. Besides, surface and vertical microstructures of specimens were characterized by micro-Raman spectroscopy with Raman imaging microscope at room temperature. The wavelength of the exciting laser beam was 785 nm. The areas for surface and vertical mappings were 150 μm × 150 μm and 30 μm × 30 μm, respectively.

To gain more information about the nanoscale phase structure, X-ray energy-dispersive spectroscopy (EDS) analysis was conducted to verify the distribution of fluorine (F) element using Tescan MIRA LMS scanning electron microscope (SEM). Prior to the test, the sample surface was coated by palladium sputtering.

The distribution of conductive component was detected by the PeakForce TUNA^{TM} mode of the atomic force microscope (AFM, Multimode 8, Bruker, Germany). The reaction mixture was dropped onto a specimen stage to give a smooth flat surface and coupled with the instrument by conductive silver paste.

X-ray diffractograms of the samples were recorded using Cu-K_α radiation (D-MAX 2200 VPC, X-ray Diffractometer, Japan).

Small angle X-ray scattering (SAXS) spectra were collected with a Bruker Nanostar X-ray scatter meter (Bruker, Germany). The scattering vector, q, changed between 0.01 and 2.1 nm^{-1}.

Wide-angle X-ray scattering (WAXS) spectrum was measured by Eiger2R 1M detector (Xeuss 3.0, Xenocs, France) with CuK_α (λ=1.5418 Å). The scattering vector, q, changed between 1 and 30 nm^{-1}. The distance from the detector to the sample was 60 mm and the exposure time was 480 s.

X-ray electron spectroscopy spectra was recorded with Thermo Scientific K-Alpha, where the number of energy step = 1361, pass energy = 150 eV, step size = 1 eV, sweep time = 136.1 s, and X-ray spot size = 400 μm × 400 μm.

Electrical resistance, R, was measured by a UNI-T UT136 digital multimeter at room temperature. The sample size was 20 mm × 5 mm × 0.1 mm.

Tensile stress ~ strain curves of dumbbell-shaped specimens (35 mm × 2 mm × 0.1 mm) were obtained using a CMT6103 universal tester (SANS, China) under a crosshead speed of 5 mm min^{-1}. Besides, the relative resistance variation under tension, R/R_o, was recorded using the above-mentioned multimeter at room temperature with the assistance of the same universal tester at the crosshead speed of 5 mm min^{-1}, where R_o represents the resistance of the original specimen (40 mm × 10 mm × 0.1 mm). Meanwhile, the relative resistance variation in response to bending was also characterized by means of the same equipment and specimen at the crosshead speed of 10 mm

min^{-1}, except that the grips moved in opposite directions until the specimen is bent to a radius of curvature of 1 mm.

The cyclic loading-unloading tensile tests of the dumbbell-shaped specimens (35 mm × 2 mm × 0.1 mm) were carried out on the same universal tester mentioned above at the maximum strain of 70% under the loading speed of 5 mm min^{-1} and the unloading rate of 20 mm min^{-1}. The resistances and tensile stress-strain curves of the specimens were also recorded in the course of deformation. Moreover, cyclic bending tests of the rectangular specimens (40 mm × 10 mm × 0.1 mm) were conducted in terms of an ADT-AV02 fatigue testing machine (Shimadzu). The specimen was repeatedly bent between the radius of curvature of infinity and the radius of curvature of 1 mm under a constant frequency of 0.5 Hz. During the tests, the resistances of the specimens were recorded.

Strain distributions during stretching and bending were measured by means of digital image correlation (DIC, Correlated Solutions Europe, Germany) at room temperature. The geometries of the specimens are dumbbell-shape (35 mm × 2 mm × 0.1 mm) for stretching and rectangular (40 mm × 10 mm × 0.1 mm) for bending, respectively. Prior to the experiments, surfaces of the specimens were painted to form matte white speckle patterns. Then, the specimens were clamped by the grips with a grip-to-grip separation of ~ 20 mm. The deformation of the specimens was driven by the aforesaid fatigue testing machine. The cyclic tension was applied at a frequency of 0.005 Hz and the maximum strain of 70%, and the cyclic bending was performed between the radius of curvature of infinity and the radius of curvature of 1 mm at a frequency of 0.5 Hz. The results of the strain distribution were collected from the last cyclic tests.

Self-healing ability was qualitatively and quantitatively characterized, respectively. For the former, a scratch was made on the sample surface with a razor blade. Then, the sample was kept at 150 ºC for 90 min and at 80 ºC for 6 h. The effect of repairing was inspected using a digital microscope (KEYENCE VHX-1000C). For the latter, the middle part of the dumbbell-shaped specimen was cut to a certain depth along the thickness direction (about 30% deep of the specimen thickness) and tested to failure under tension, offering tensile strength, TS_{cut}. Afterwards, another specimen, which was partially cut in the same way in advance, was healed at 150 ºC for 90 min and at 80 ºC for 6 h under gentle pressure of ~0.2 MPa. The tensile strength of the healed specimen, TS_{healed}, was determined, and the healing efficiency of strength restoration, η_{TS}, was calculated from:

$$\eta_{TS} = \frac{TS_{healed} - TS_{cut}}{TS_{virgin} - TS_{cut}} \qquad (2)$$

where TS_{virgin} denotes tensile strength of the virgin specimen. In the meantime, electrical conductivities of the virgin, cut and healed specimens, σ_{virgin}, σ_{cut} and σ_{healed}, were also measured, while rectangular specimens (20 mm × 5 mm × 0.1 mm) were used instead. The healing efficiency of conduction restoration, η_σ, was calculated from:

$$\eta_\sigma = \frac{\sigma_{healed} - \sigma_{cut}}{\sigma_{virgin} - \sigma_{cut}} \quad (3)$$

Contact angles were measured in terms of a Krüss DSA-100 drop shape analyzer using water and diiodomethane as the test liquids. Furthermore, the dispersion component, γ_S^d, and the polar component, γ_S^p, of the total surface energy, γ_S, were calculated according to Wu's method[2,3]:

$$\cos\theta = -1 + \frac{2\sqrt{\gamma_S^d \gamma_L^d}}{\gamma_L} + \frac{2\sqrt{\gamma_S^p \gamma_L^p}}{\gamma_L} \quad (4)$$

where θ is the measured contact angle, and γ_L, γ_L^d and γ_L^p are the total surface free energy, dispersion component, and polar component of the test liquid, respectively. γ_S can thus be obtained from:

$$\gamma_S = \gamma_S^p + \gamma_S^d \quad (5)$$

Fractional free volume and pore radius of the materials were investigated using a positron annihilation lifetime spectrometer (PALS, ORTEC 0107A) with ^{22}Na as the radiation source. The quantitative relation between orthopositronium (o-Ps) lifetimes (τ_3) and cavity radius of free volume (r) is described as follows[4]:

$$\tau_3 = \frac{1}{2}\left[1 - \frac{r}{r_0} + \frac{1}{2\pi}\sin\left(\frac{2\pi r}{r_0}\right)\right]^{-1} \quad (6)$$

where $r_0 = r + r_\delta$. r_δ is a semi-empirical constant, 1.656×10^{-1} nm. Assuming that the free volume hole is spherical, its volume, V_f, can be estimated by:

$$V_f = \frac{4}{3}\pi r^3 \quad (7)$$

The fractional free volume, F_R, is given by:

$$\mathrm{F}_R = \mathrm{C} \times V_f \times I_3 \quad (8)$$

where I_3 is the intensity (%) of the o-Ps, and C is an empirical constant (0.018 nm^{-3})[5].

To assess the transport mechanism involved according to Mott's variable range hopping (VRH) theory, temperature dependences of electrical conductivity of the rectangular specimens were measured between 280 and 325 K and fitted with the VRH model.

The short-circuit currents of the assembled triboelectric nanogenerator (TENG) during finger motion under the circumstances of RH = 50%, 90% and artificial sweat infiltration were recorded by an electrochemical workstation (CHI 760E, Shanghai, China) at ambient temperature, respectively.

1.2 Statistical analysis

Quantitative data were described in the form of means ± standard deviation, such as the error bars in the figures. At least three samples were conducted to test the average mechanical properties, electrical resistance/conductivity. All statistical analyses were carried out with the Origin software package.

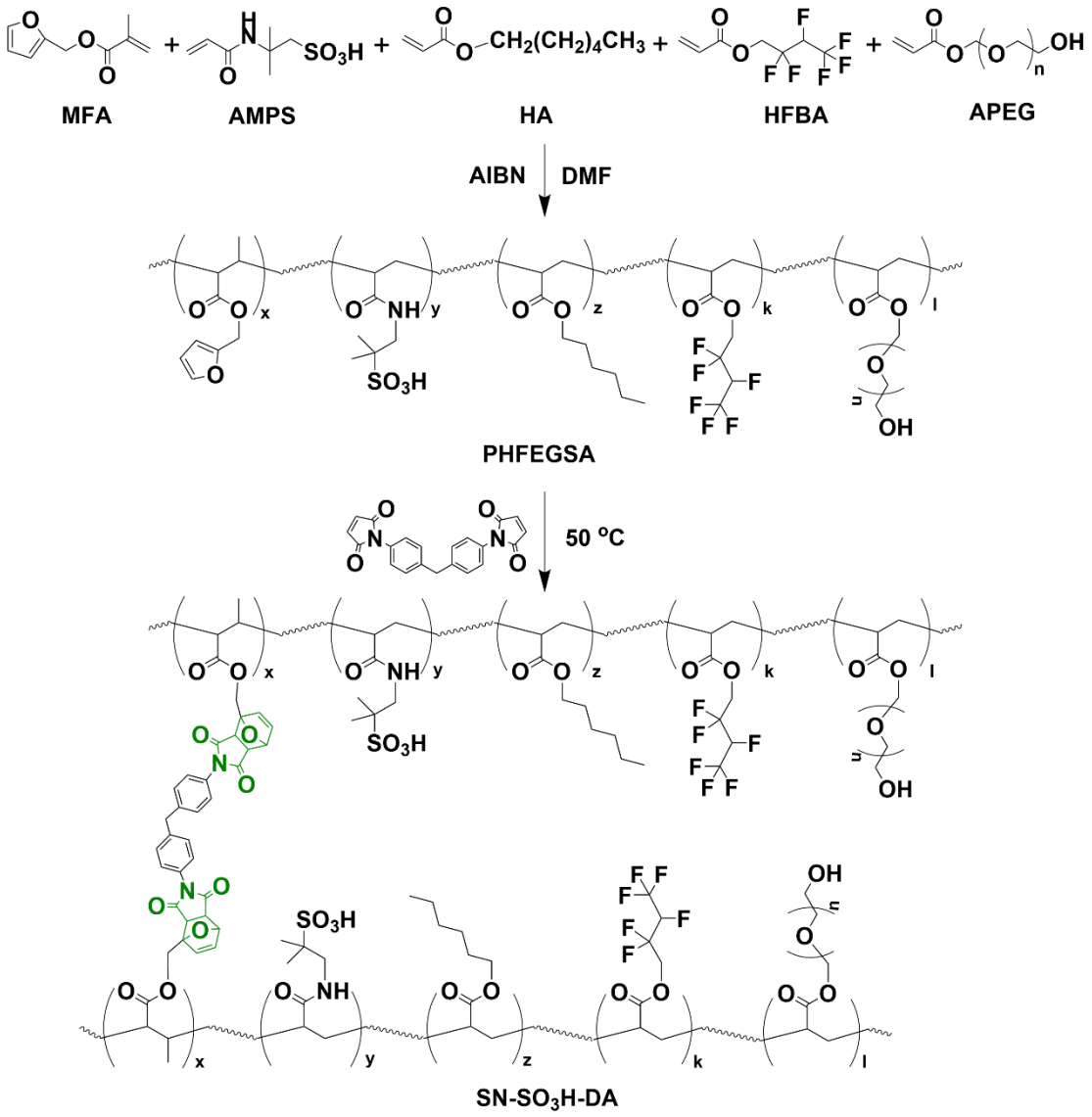

Fig. S1. Synthesis of SN-SO_3H-DA.

On the whole, there were six components of SN-SO_3H-DA: MFA, BMI, AMPS, HA, APEG, and HFBA. (i) MFA and BMI are used to form Diels-Alder (DA) bonds, which are common combinations for DA bond preparation. (ii) AMPS contains both vinyl and sulfonic acid groups, of which the vinyl group is responsible for free-radical polymerization and the sulfonic acid group is

the key to SN-SO_3H-DA, as described below. By exploiting the competition between the sulfonic acid group/PEDOT and PSS/PEDOT interactions, PSS can be easily separated from PEDOT:PSS, and SN-SO_3H-DA serves as a substitute for PSS, thus, enabling the alignment of PEDOT along the SN-SO_3H-DA chains. Meanwhile, the sulfonic acid group increased the water solubility of SN-SO_3H-DA, which helped homogeneously mix the dissociated SN-SO_3H-DA with PEDOT:PSS in water. This is a prerequisite for preparing desired interlocking networks. (iii) Because flexible materials must have low glass transition temperatures, HA was chosen to reduce the glass transition temperature of SN-SO_3H-DA because of its relatively long alkane chains. HA is a free-radical polymerization monomer commonly used for preparing polymers with low glass transition temperatures (T_g). (iv) APEG can simultaneously increase the water solubility of SN-SO_3H-DA and decrease its T_g. Because AMPS contains a sulfonic acid group, excess AMPS increases the glass transition temperature of the material, turning it into a rigid material. In this context, the amount of AMPS should be appropriately adjusted to balance water solubility and T_g. In addition, APEG can undergo free-radical polymerization. (v) HFBA improved the elongation at break and strength of SN-SO_3H-DA. Because of the high content of fluorine atoms in HFBA, only a small amount must be added to ensure that the T_g and strength of SN-SO_3H-DA meet our requirements without affecting the water solubility and glass transition temperature. Moreover, HFBA contains vinyl groups that can be involved in free-radical polymerization.

The chemical structure of the resultant SN-SO_3H-DA is verified by the FTIR spectrum in **Fig. S2a**, which shows the characteristic peaks at 1725 cm^{-1} (C=O, stretching), 1545 cm^{-1} (-CONH, bending), 1228 cm^{-1} (C-F, stretching), 1105 cm^{-1} (C-O-C of ester group, stretching) and 1035 cm^{-1} (S=O of -SO_3H, stretching). The presence of DA adduct in SN-SO_3H-DA is further proved by the appearance of the peak at 1781 cm^{-1} (i.e. the DA adduct of maleimide) on the FTIR spectrum and the endothermic peak originating from the re-DA reaction on the DSC heating curve (**Fig. S2b**)[6,7]. Furthermore, the M_c of SN-SO_3H-DA was estimated to be ~7600 g mol^{-1} according to the result of DMA (**Fig. S2c**) and Equation 1.

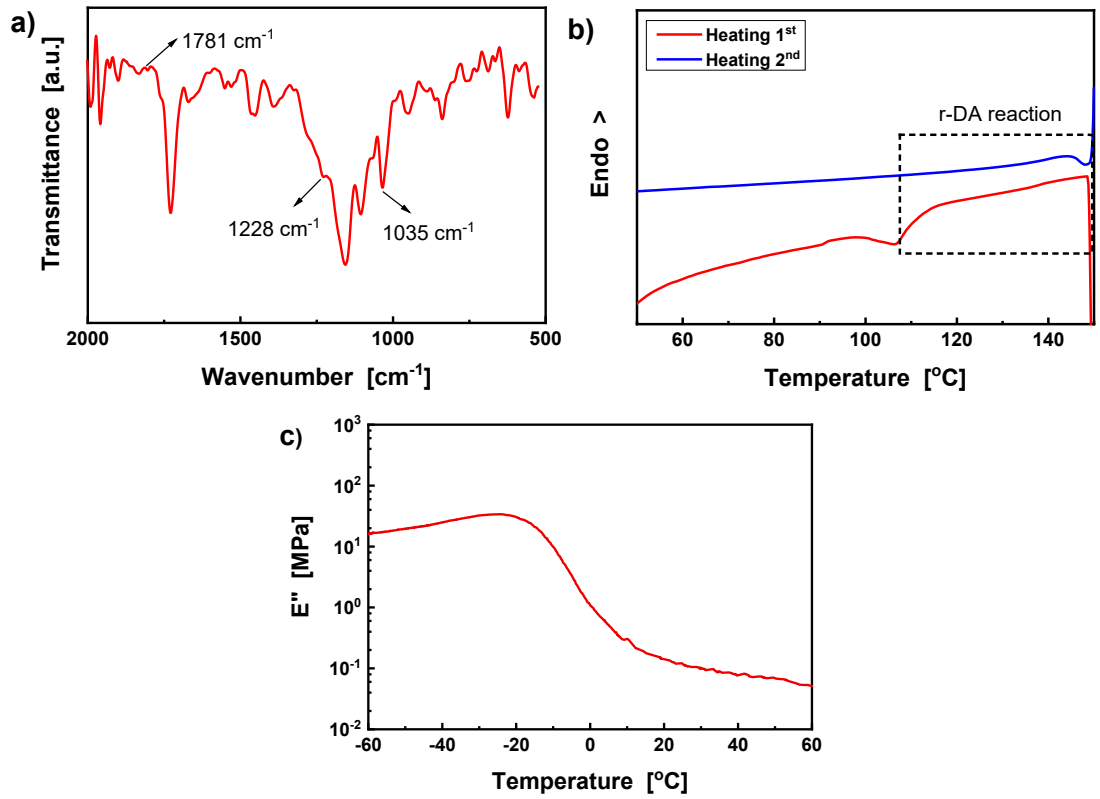

Fig. S2. Characterization of SN-SO$_3$H-DA. (a) FTIR spectrum, (b) DSC heating curve (heating rate: 10 ºC min^{-1}) and (c) temperature dependence of loss modulus, *E''*, of SN-SO$_3$H-DA.

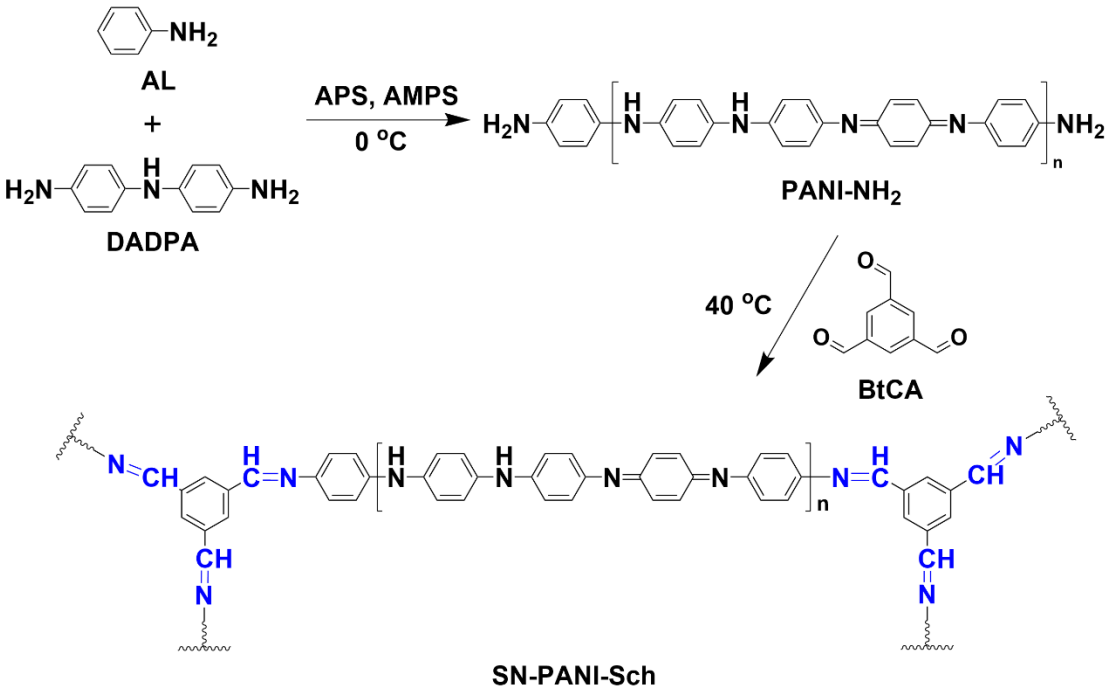

Fig. S3. Synthesis of SN-PANI-Sch.

The ^{1}H NMR spectrum of the PANI-NH_2 sample[8] is shown in **Fig. S4a**. Three sharp and equidistant peaks can be clearly identified at chemical shifts of 6.95, 7.07 and 7.21 ppm, respectively, attributing to N^{+}-*H* of the doping protons of PANI-NH_2.[9] Considering that PANI with high polymerization degree cannot be dissolved and perform the indispensable liquid-phase reaction for producing RILNs, the polymerization degree of PANI-NH_2 has to be controlled below 15 accordingly. The MALDI-TOF-MS spectrum in **Fig. S4b** indicates that the molecular chain of PANI-NH_2 is terminated by two amines, and the degree of polymerization is mainly 4, 5, 8, and 9 in line with the above expectation. Accordingly, it can be inferred that the M_c of SN-PANI-Sch is ~600 g mol^{-1}.

The chemical structure of SN-PANI-Sch is examined by FTIR spectrum (**Fig. S4c**) as characterized by the peaks at 3316 cm^{-1} (N-H, stretching), 1617 cm^{-1} (C=N of Shiff base, stretching), 1573 cm^{-1} (C=C of benzoquinone, stretching), 1284 cm^{-1} (C-C, bending vibration), and 1215 cm^{-1} (C-N, stretching)[10,11]. Besides, the result of ^{13}C CP/MAS (**Fig. S4d**) well agrees with that of the FTIR. The peak at 120.2 ppm is assigned to benzene ring (C-2, C-3, C-5, C-6), while that at 125.4 ppm results from the quinoid ring (C-8, C-9, C-11, C-12). The peaks at 140.7 ppm and 156.3 ppm are attributed to C-1, C-10 and C-13 of -C=N.[12,13] Finally, the C-C stretching at 1511 cm^{-1}, and C-N^{+} stretching at 1334 cm^{-1} and 1394 cm^{-1} of quinoid ring also validate the structure of SN-PANI-Sch (**Fig. S4e**).[14,15]

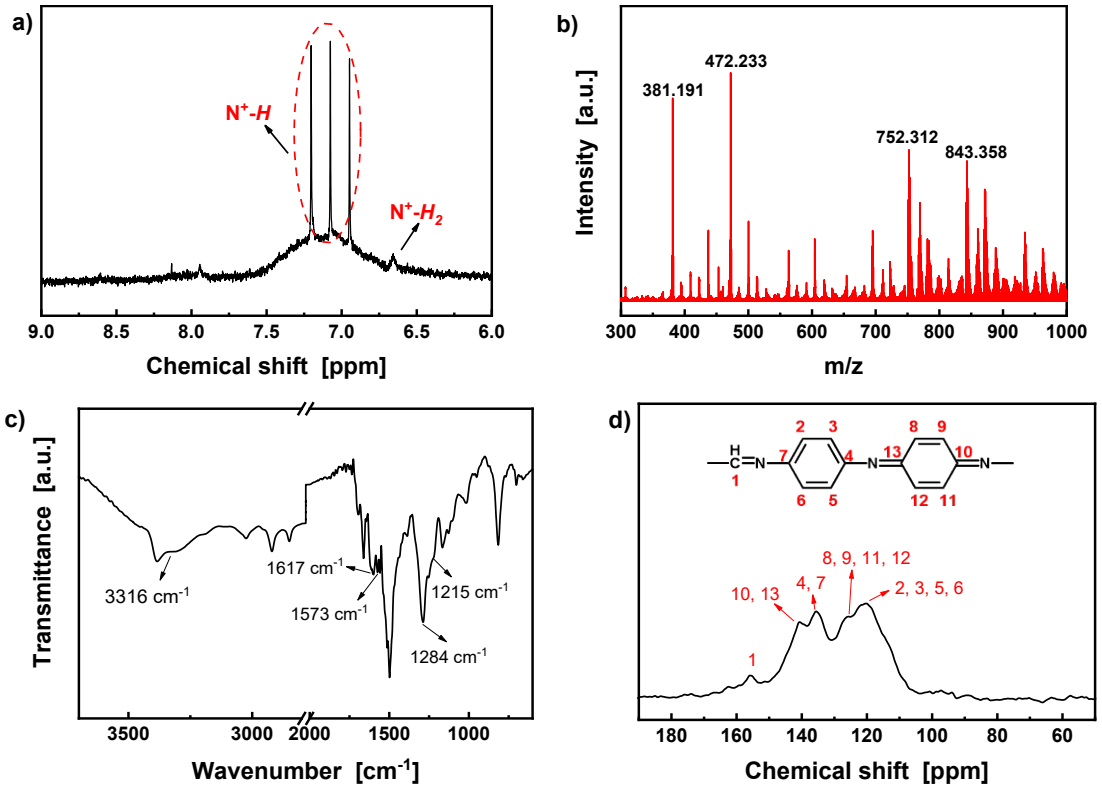

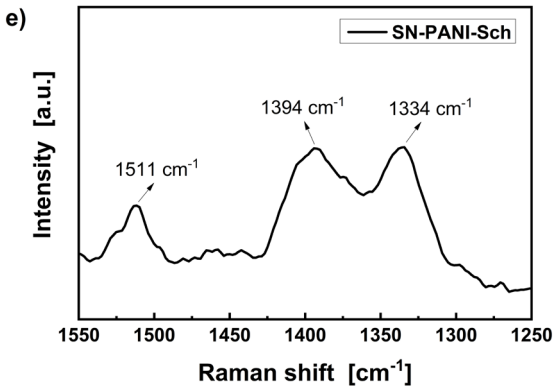

Fig. S4. Characterization of PANI-NH_2 and SN-PANI-Sch. (a) ^{1}H NMR and (b) MALDI-TOF-MS spectra of PANI-NH_2. (c) FTIR, (d) ^{13}C CP/MAS and (e) Raman spectra of SN-PANI-Sch.

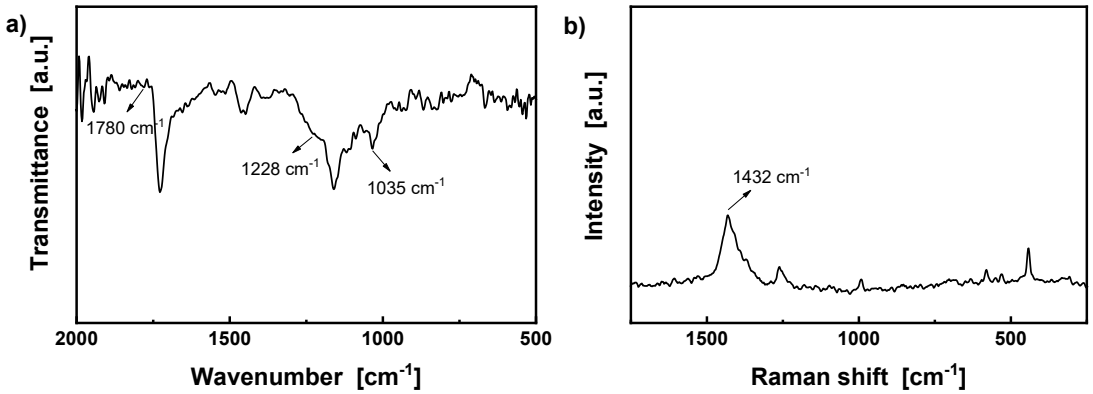

Fig. S5. Characterization of PEDOT/RILNs. (a) FTIR and (b) Raman spectra of PEDOT/RILNs (contents of PEDOT, SN-PANI-Sch and SN-SO_3H-DA are 3.08, 0.27 and 96.65 wt%, respectively).

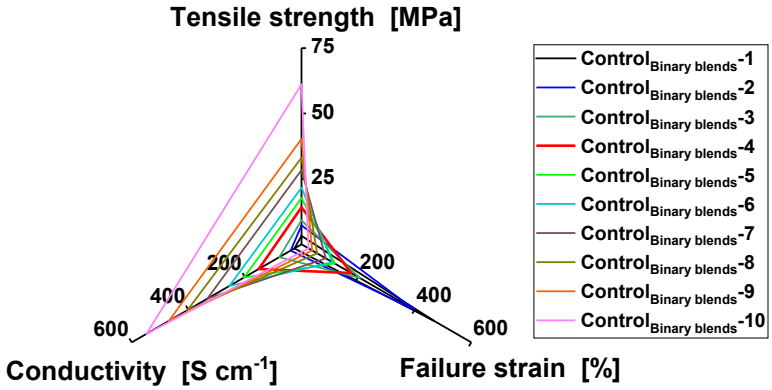

Fig. S6. Conductivities, tensile strengths, and failure strains of $Control_{Binary\ blends}$ (The blends consist of PEDOT and SN-SO_3H-DA with PEDOT contents from 0.73 - 30.02 wt%, refer to **Table S1**).

Table S1. Compositions of the target conducting polymer films and the controls

PEDOT/RILNs

Sample ID	PEDOT (wt%)	SN-PANI-Sch (wt%)	SN-SO_3H-DA (wt%)
PEDOT/RILNs-1	1.48	0.13	98.39
PEDOT/RILNs-2	3.08	0.27	96.65
PEDOT/RILNs-3	6.67	0.58	92.75
PEDOT/RILNs-4	10.92	0.95	88.13
PEDOT/RILNs-5	16.01	1.40	82.59
PEDOT/RILNs-6	22.24	1.94	75.82

$Control_{Binary\ blends}$

Sample ID	PEDOT (wt%)	SN-SO_3H-DA (wt%)
$Control_{Binary\ blends}$-1	0.73	99.27
$Control_{Binary\ blends}$-2	1.48	98.52
$Control_{Binary\ blends}$-3	2.27	97.73
$Control_{Binary\ blends}$-4	3.08	96.92
$Control_{Binary\ blends}$-5	4.80	95.20
$Control_{Binary\ blends}$-6	6.67	93.33
$Control_{Binary\ blends}$-7	10.92	89.08
$Control_{Binary\ blends}$-8	16.01	83.99
$Control_{Binary\ blends}$-9	22.24	77.76
$Control_{Binary\ blends}$-10	30.02	69.98

$Control_{Ternary\ blends}$

Sample ID	PEDOT (wt%)	SN-PANI-Sch (wt%)	Polysulfonic acid (wt%)
$Control_{Ternary\ blends}$-1	1.48	0.13	98.39
$Control_{Ternary\ blends}$-2	3.08	0.27	96.65
$Control_{Ternary\ blends}$-3	6.67	0.58	92.75
$Control_{Ternary\ blends}$-4	10.92	0.95	88.13
$Control_{Ternary\ blends}$-5	16.01	1.40	82.59
$Control_{Ternary\ blends}$-6	22.24	1.94	75.82

Control'$_{Ternary\ blends}$

Sample ID	PEDOT (wt%)	PANI-NH_2 (wt%)	SN-SO_3H-DA (wt%)
Control'$_{Ternary\ blends}$-1	1.48	0.13	98.39
Control'$_{Ternary\ blends}$-2	3.08	0.27	96.65
Control'$_{Ternary\ blends}$-3	6.67	0.58	92.75
Control'$_{Ternary\ blends}$-4	10.92	0.95	88.13

Control'$_{\text{Ternary blends}}$-5	16.01	1.40	82.59
Control'$_{\text{Ternary blends}}$-6	22.24	1.94	75.82
Synchronous IPNs			
Sample ID	PEDOT (wt%)	PANI-NH_2 (wt%)	SN-SO_3H-DA & GTE (wt%)
Synchronous IPNs-1	3.08	0.27	96.65
Synchronous IPNs-2	3.08	2.15	94.77
Sequential IPNs			
Sample ID	PEDOT (wt%)	SN-PANI-Sch (wt%)	SN-SO_3H-DA (wt%)
Sequential IPNs	3.08	0.27	96.65

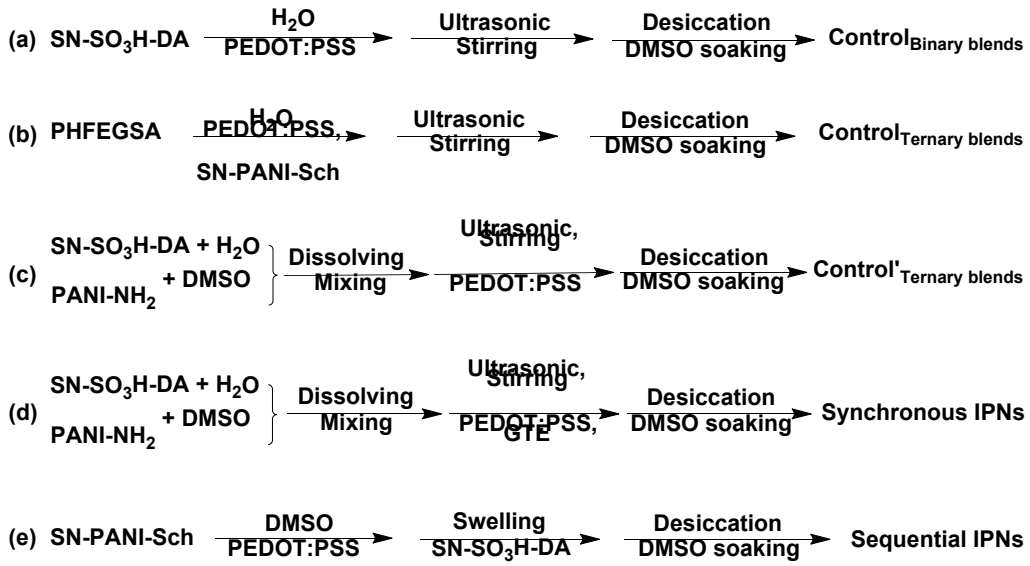

Fig. S7. Synthesis of (a) Control$_{\text{Binary blends}}$, (b) Control$_{\text{Ternary blends}}$, (c) Control'$_{\text{Ternary blends}}$, (d) synchronous IPNs and (e) sequential IPNs.

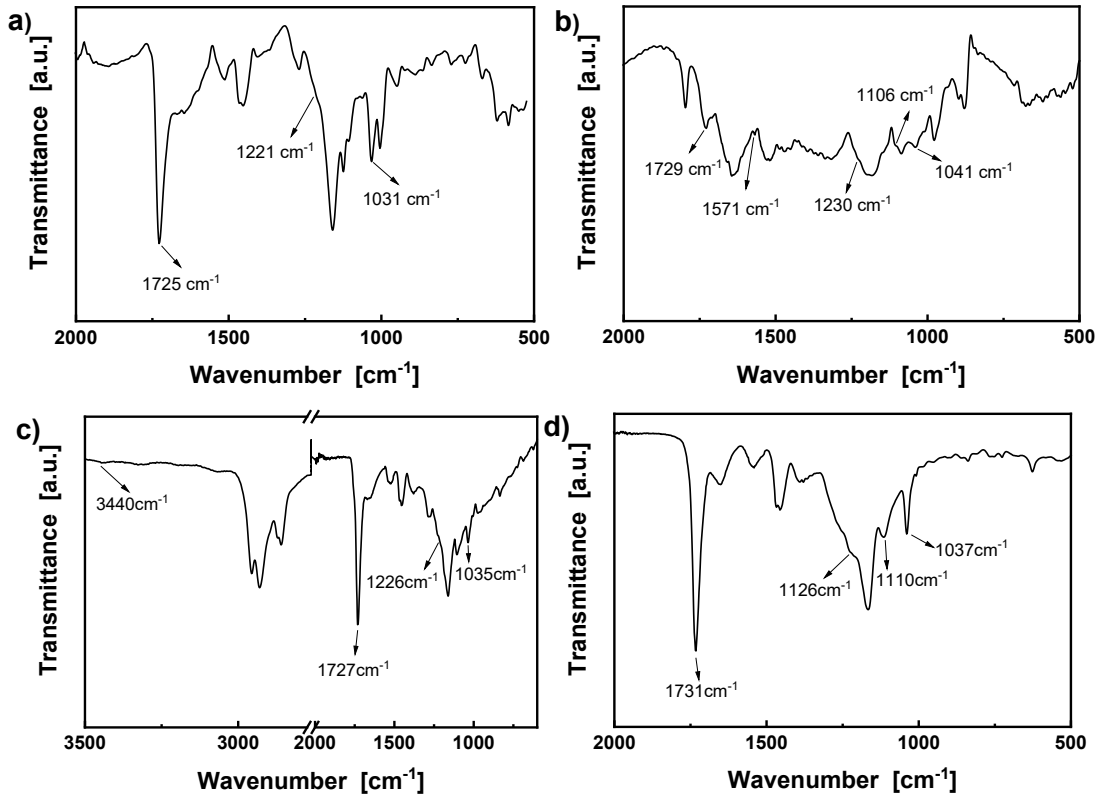

Fig. S8. FTIR spectra of (a) $Control_{Binary\ blends}$-4, (b) $Control_{Ternary\ blends}$-2, (c) $Control'_{Ternary\ blends}$-2, and (d) synchronous IPNs-2.

The FTIR spectrum of $Control_{Binary\ blends}$ represented by $Control_{Binary\ blends}$-4 in **Fig. S8a** suggests that this type of controls has been successfully prepared, which is evidenced by the characteristic peaks at 1725 cm^{-1} (C=O, stretching), 1221 cm^{-1} (C-F, stretching), and 1031 cm^{-1} (S=O of $-SO_3H$, stretching). Meantime, the chemical structure of $Control_{Ternary\ blends}$-2 is proved by the FTIR spectrum in **Fig. S8b**. The characteristic peaks are perceived at 1729 cm^{-1} (C=O, stretching), 1571 cm^{-1} (C=C of quinone of PANI, stretching), 1230 cm^{-1} (C-F, stretching), 1106 cm^{-1} (C-O-C of ester group, stretching) and 1041 cm^{-1} (S=O of $-SO_3H$, stretching), respectively. Besides, the characteristic peaks of $Control'_{Ternary\ blends}$-2 in **Fig. S8c** are found at 3440 cm^{-1} (NH_2 of PANI, stretching), 1727 cm^{-1} (C=O, stretching), 1226 cm^{-1} (C-F, stretching) and 1035 cm^{-1} (S=O of $-SO_3H$, stretching), respectively. As for the synchronous IPNs, which are represented by synchronous IPNs-2, their successful production is confirmed by the FTIR peaks at 1731 cm^{-1} (C=O, stretching), 1226 cm^{-1} (C-F, stretching), 1110 cm^{-1} (C-O-C of ester group, stretching) and 1037 cm^{-1} (S=O of $-SO_3H$, stretching), respectively (**Fig. S8d**).

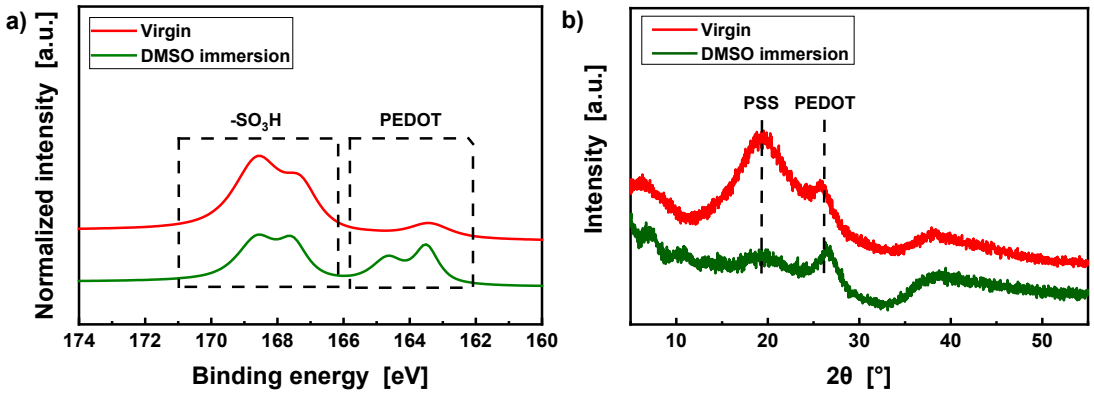

Fig. S9. Composition variation in PEDOT/RILNs-2 before and after DMSO immersion. (a) The high-resolution XPS spectra of PEDOT/RILNs-2 before and after DMSO immersion showing the S(2p) peaks of PEDOT and PSS. Note: Due to the spin-orbit coupling, the S(2p) peak is a doublet S($p_{1/2, 3/2}$). That is, the S signals for the sulphonate group of PSS in the high binding energy region (~168.5 and ~167.0 eV), and the S signals of PEDOT at the low binding energy region (~163.0 and ~164.6 eV). (b) XRD spectra of PEDOT/RILNs-2 before and after DMSO immersion showing the PEDOT and PSS peaks.

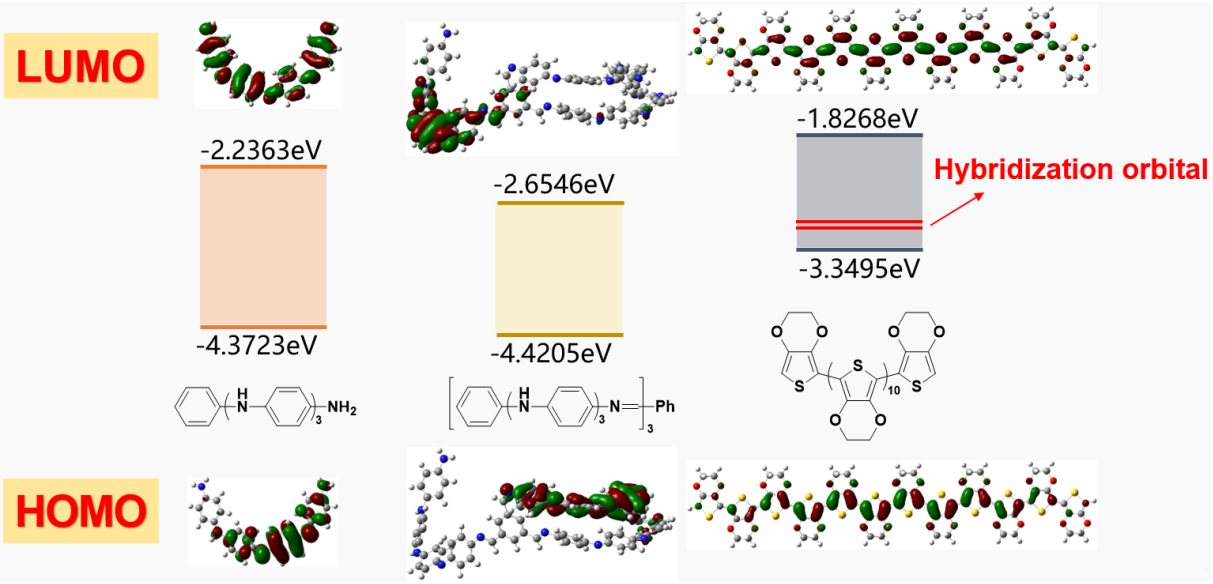

Fig. S10. Electron density distributions of HOMO and LUMO levels.

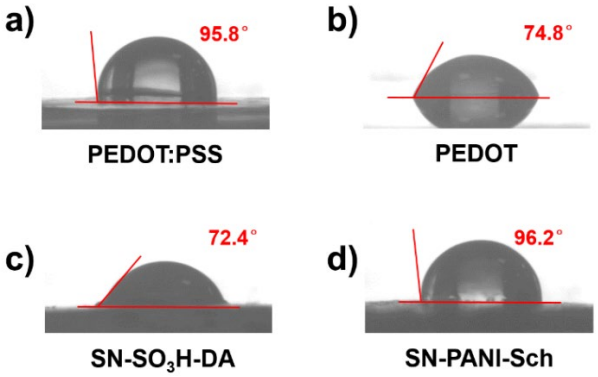

Fig. S11. Images showing water contact angles of (a) PEDOT:PSS, (b) PEDOT (PEDOT:PSS soaked in DMSO for 9 h in advance), (c) SN-SO_3H-DA and (d) SN-PANI-Sch.

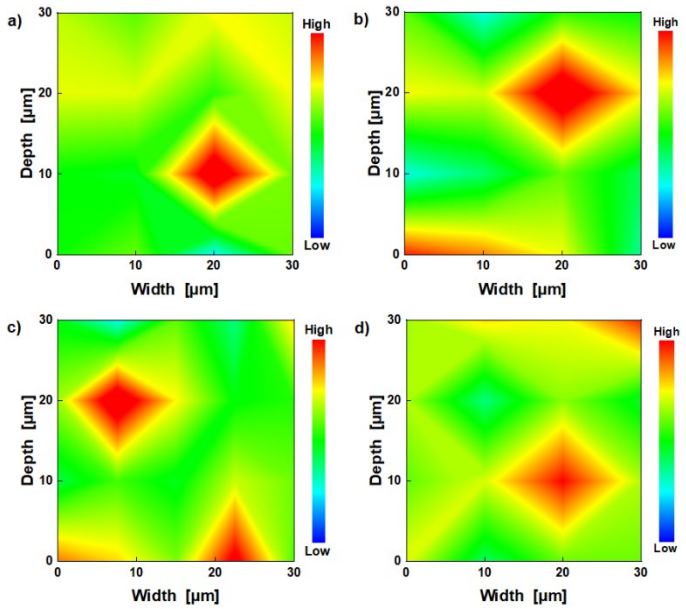

Fig. S12. Characterization of internal and external structural consistency of PEDOT/RILNs-5. Micro-Raman spectroscopy analysis of the distribution of the benzene ring (approximately 1500 cm^{-1}) of SN-PANI-Sch along the vertical direction of PEDOT/RILNs-5. Sample thickness: (a, b) approximately 60 μm; (c, d) approximately 110 μm. Inspection surface: (a, c) The side facing outward when molded; (b, d) The side facing inward when molded. Note: Because of the limited effective scanning depth of the instrument (approximately 30 μm), we checked the filmy samples of different thicknesses as well as the two sides of the films to ensure an accurate interpretation.

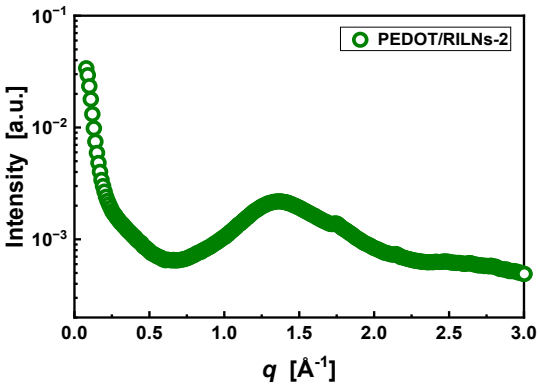

Figure S13. WAXS spectrum of PEDOT/RILNs-2.

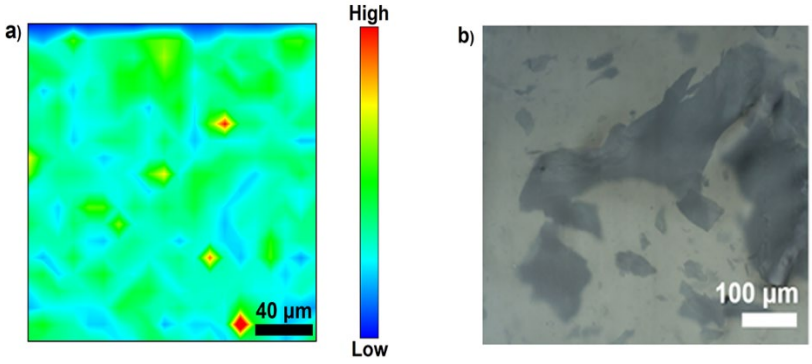

Fig. S14. Homogeneity characterization of the IPNs. (a) Micro-FTIR spectroscopy analysis of the distribution of the benzene ring (approximately 1500 cm^{-1}) of PANI on the surface of synchronous IPNs-2. (b) Light microscopic image of the sequential IPNs.

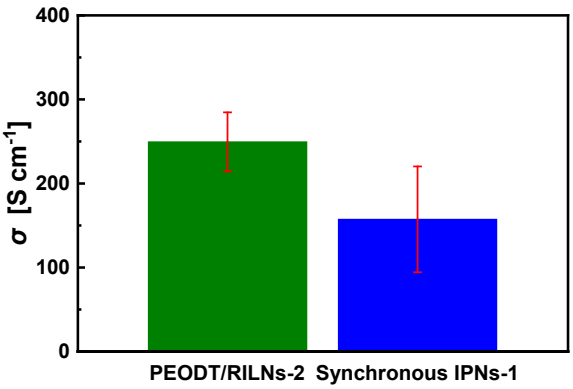

Fig. S15. Conductivities of PEDOT/RILNs-2 and synchronous IPNs-1 containing fixed contents of PEDOT (3.08 wt%) and PANI (0.27 wt%). Note: Conductivity of sequential IPNs could not be offered due to the unacceptable measurement deviations caused by the severe phase separation.

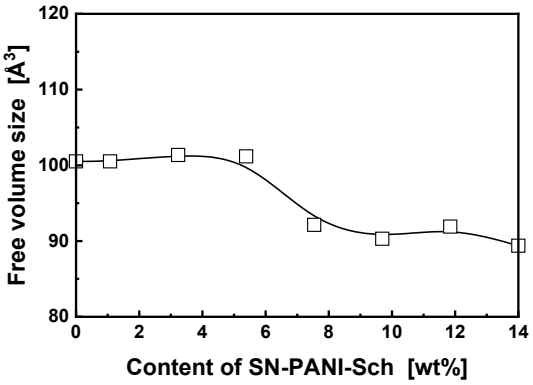

Fig. S16. Free volume size of PEDOT/RILNs as a function of content of SN-PANI-Sch.

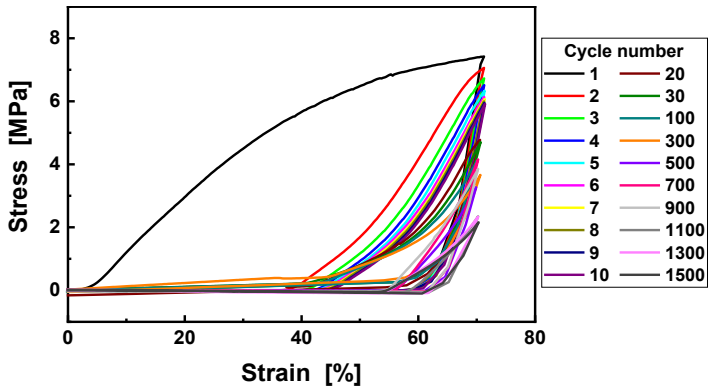

Fig. S17. Cyclic tensile curve of PEDOT/RILNs-2 for 1500 times with maximum strain of 70%.

Table S2. Comparison of the maximum tensile strains at zero relative resistance change of the strain-insensitive flexible conductive materials reported in literature and that of PEDOT/RILNs-2

Materials*	**Maximum tensile strain at $\Delta R/R_o$** ≈ 0**	**Ref.**
PEDOT:PSS/PAAMPSA/EMIMOTF	20%	[16]
PEDOT/PSS-*b*-PPEGMEA	15%	[17]
SEBS supported PEDOT:PSS/PEO20-PPO70-PEO20	10%	[18]
Prestretched (30%) PEDOT:PSS/PU/1wt% rGO	10%	[19]
Ag nanoparticle deposited on wavy PDMS	10%	[20]
PU supported AgNWs mesh	50%	[21]
Prestretched (50%) PDMS supported AgNWs/PEDOT:PSS	10%	[22]
SEBS supported serpentine Ag-EGaInPs	80%	[23]
Serpentine Au/PDMS	65%	[24]
CNTs/PU foam/silicone	5%	[25]

Pyrolyzed BC/PDMS	10%	[26]
SWCNTs aerogel/PDMS	30%	[27]
Prestretched (120%) PDMS supported reticulate SWNTs	140%	[28]
PEDOT:PSS/acrylamide organogels	20%	[29]
SEBS supported PEDOT:PSS/PR-PEGMA	10%	[30]
SEBS supported PEDOT:PSS/organic plasticizer	5%	[31]
PDMS supported PEDOT:PSS/PU	20%	[32]
PUF/PEDOT/PDMS	20%	[33]
PEDOT/RILNs-2	125%	This work

*PR-PEGMA: polyrotaxane-polyethylene glycol methacrylate. SEBS: styrene-ethylene-butylenestyrene. PU: polyurethane. PSS-*b*-PPEGMEA: poly(styrenesulfonate)-b-poly(poly(ethylene glycol) methyl ether acrylate). PAAMPSA: poly(2-acrylamido-2-methyl-1-propanesulfonic acid. EMIMOTF: 1-ethyl-3-methylimidazolium-trifluoromethanesulfonate, PUF: polyurethane fiber mat. PDMS: poly(dimethylsiloxane). PEO20-PPO70-PEO20: poly(ethylene glycol)-*b*-poly(propylene glycol)-*b*-poly(ethylene glycol). CNTs: carbon nanotubes. rGO: reduced graphene oxide. AgNWs: silver nanowires. EGaInPs: eutectic gallium-indium particles. BC: bacterial cellulose. SWCNTs: single-walled carbon nano tubes.
**$\Delta R = R - R_o$, where R and R_o are the real time and initial resistance, respectively.

Table S3. Comparison of self-healing ability and the maximum cyclic stretching/bending numbers at zero change in electrical properties of flexible conducting polymers

Materials*	Self-healability	Maximum cyclic stretching number at zero change in electrical properties**	Maximum cyclic bending number at zero change in electrical properties**	Ref.
PEDOT/PSS-b-PPEGMEA	Yes	210 [*R*, 7%]	N.A.	[19]
SEBS supported PEDOT:PSS/PEO20-PPO70-PEO20	N.A.	1 [*R*, 40%]	N.A.	[24]
TPU supported PEDOT:PSS	N.A.	1 [*R*, 30%]	N.A.	[34]
Prestretched (30%) PEDOT:PSS/PU/1wt% rGO	N.A.	200 [*R*, 30%]	N.A.	[35]
PDMS supported PEDOT:PSS/EMIM TCB	N.A.	10 [Luminance, 40%]	N.A.	[20]
PDMS supported PEDOT:PSS/EMIM DCI and EMIM DCA	N.A.	10 [σ, 30%]	N.A.	[18]
PET supported PEDOT	N.A.	N.A.	1500 [R, 5.3 mm]	[36]
PPy/PDMS	N.A.	N.A.	500 [σ, N.A.]	[28]
PU supported Ag/PTFE	N.A.	20 [*R*, 20%]	1000 [R, 1 mm]	[37]
PET supported PEDOT:PSS/AgNWs	N.A.	N.A.	10 [R, 3 mm]	[38]
PEDOT:PSS on textile	N.A.	50 [*R*, 30%]	50 [R, 11 mm]	[39]
PDMS supported WO_3/AgNNs/PEDOT:PSS/WO_3	N.A.	N.A.	1000 [R, 0.5 mm]	[40]

PEDOT:PSS/NOA63	N.A.	N.A.	1000 [J_{sc}, 1 mm]	[41]
PDMS supported PEDOT:PSS	N.A.	N.A.	200 [R, 4 mm]	[42]
PDMS supported PEDOT:PSS/PU	N.A.	10 [*R*, 50%]	N.A.	[43]
PDMS supported Prestretched (50%) PDMS supported AgNWs/PEDOT:PSS	N.A.	50 [*R*, 50%]	N.A.	[44]
PDMS supported PEDOT:PSS/rGO	N.A.	55 [*R*, 15%]	N.A.	[45]
PEDOT:PSS on stretchable textile	N.A.	50 [*R*, 30%]	N.A.	[46]
PEDOT:PSA/PAA hydrogel	N.A.	1 [*R*, 50%]	N.A.	[47]
PANI/PAAMPSA/PA	Yes	30 [Thermovoltage, 50%]	N.A.	[48]
PU supported CNTs	Yes	50 [Transfer characteristics, 50%]	N.A.	[49]
PEDOT/RILNs-2	Yes	500 [*R*, 70%]	10^6 [R, 1 mm]	This work

*EMMI TCB: 1-ethyl-3-methylimidazolium tetracyanoborat. EMIM DCI: 1-ethyl-3-methylimidazolium 4,5-dicyanoimidazolate. EMIM DCA: 1-ethyl-3-methylimidazolium dicyanamide. TPU: thermoplastic polyurethane. PSA: polystyrene sulfonate-co-acrylic acid). PAA: polyacrylic acid. PTFE: polytetrafluoroethylene. NOA63: noland optical adhesive 63. PET: polyethylene glycol terephthalate. PPy: polypyrrole. WO_3: tungsten trioxide. AgNNs: silver nanotrough networks.

**The notes in the square brackets represent (i) the electrical properties used for characterizing their changes during cyclic tensile and bending deformation, and (ii) the maximum strains of the specimens for cyclic stretching or the minimum radius of curvature of the specimens for cyclic bending. *R* means electrical resistance, σ electrical conductivity, and J_{sc} short-circuit current density.

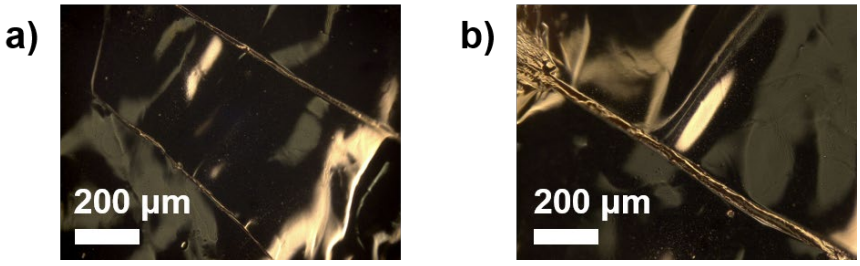

Fig. S18. Surface appearances of the SN-SO_3H-DA film coated with PEDOT:PSS after (a) repeated loading-unloading stretching for 20 cycles (maximum strain = 70%) and (b) repeated loading-unloading bending for 5 cycles (minimum radius of curvature = 1 mm).

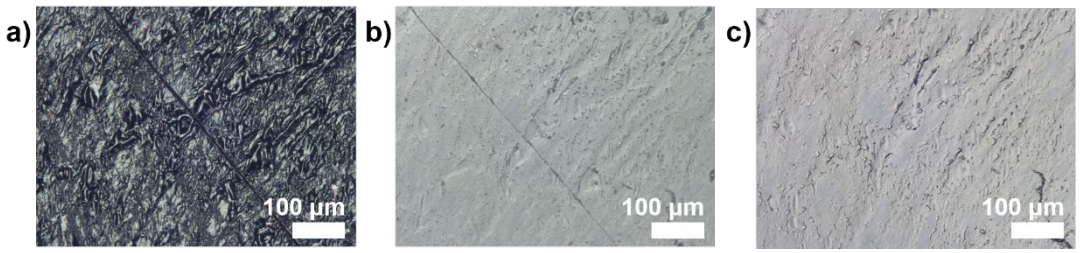

Fig. S19. Visual inspection of the self-healing behavior of PEDOT/RILNs-2. (a) Scratched sample, (b) healed sample (healing conditions: 150 ºC, 60 min), and (c) healed sample (healing conditions: 150 ºC, 90 min).

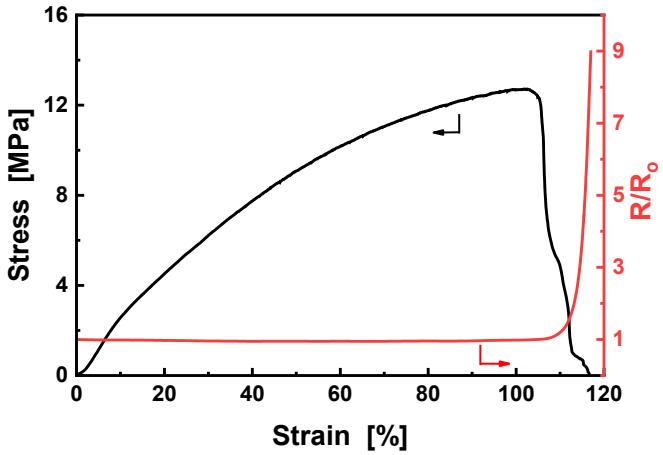

Fig. S20. Resistance variation of the healed PEDOT/RILNs-2 during stretching.

Supporting References

1. L. F. Fan, Y. N. Huang, M. Z. Rong, M. Q. Zhang and X. D. Chen, *ACS Macro Lett.*, 2019, **8**, 1141-1146.
2. S. C. H. Kwok, J. Wang and P. K. Chu, *Diam. Relat. Mater.*, 2005, **14**, 78-85.
3. S. M. Cohen and M. Muthukumar, *J. Chem. Phys.*, 1989, **90**, 5749-5755.
4. P. N. Patil, S. K. Rath, S. K. Sharma, K. Sudarshan, P. Maheshwari, M. Patri, S. Praveen and P. Khandelwal, *Soft Matter*, 2013, **9**, 3589-3599.
5. Y. Y. Wang, H. Nakanishi, Y. C. Jean and T. C. Sandreczki, *J. Polym. Sci. Pol. Phys.*, 1990, **28**, 1431-1441.
6. Y. You, W. L. Peng, P. Xie, M. Z. Rong, M. Q. Zhang and D. Liu, *Mater. Today*, 2020, **33**, 45-55.
7. Q. Tian, Y. C. Yuan, M. Z. Rong and M. Q. Zhang, *J. Mater. Chem.*, 2009, **19**, 1289-1296.

8. L. Chen, Y. Yu, H. Mao, X. Lu, W. Zhang and Y. Wei, *Mater. Lett.*, 2005, **59**, 2446-2450.
9. X. Wang, T. Sun, C. Wang, C. Wang, W. Zhang and Y. Wei, *Macromol. Chem. Phys.*, 2010, **211**, 1814-1819.
10. O. Catanescu, M. Grigoras, G. Colotin, A. Dobreanu and C. I. Simionescu, *Eur. Polym. J.*, 2001, **37**, 2213-2216.
11. S. Quillard, G. Louarn, S. Lefrant and A. G. Macdiarmid, *Phys. Rev. B: Condens. Matter.*, 1994, **50**, 12496-12508.
12. S. Kaplan, E. M. Conwell, A. F. Richter and A. G. Macdiarmid, *J. Am. Chem. Soc.*, 2002, **110**, 7647-7651.
13. Z. D. Zujovic, M. R. Gizdavic-Nikolaidis, P. A. Kilmartin, H. Idriss, S. D. Senanayake and G. A. Bowmaker, *Polymer*, 2006, **47**, 1166-1171.
14. M. Baibarac, I. Baltog and S. Lefrant, *J. Solid State Chem.*, 2009, **182**, 827-835.
15. A. Kumar, A. Mishra, K. Awasthi and V. Kumar, *Macromol. Symp.*, 2015, **357**, 168-172.
16. Y. Jiang, Z. Zhang, Y.-X. Wang, D. Li, C.-T. Coen, E. Hwaun, G. Chen, H.-C. Wu, D. Zhong, S. Niu, W. Wang, A. Saberi, J.-C. Lai, Y. Wu, Y. Wang, A. A. Trotsyuk, K. Y. Loh, C.-C. Shih, W. Xu, K. Liang, K. Zhang, Y. Bai, G. Gurusankar, W. Hu, W. Jia, Z. Cheng, R. H. Dauskardt, G. C. Gurtner, J. B.-H. Tok, K. Deisseroth, I. Soltesz and Z. Bao, *Science*, 2022, **375**, 1411-1417.
17. H. He, L. Zhang, S. Yue, S. Yu, J. Wei and J. Ouyang, *Macromolecules*, 2021, **54**, 1234-1242.
18. J. H. Lee, Y. R. Jeong, G. Lee, S. W. Jin, Y. H. Lee, S. Y. Hong, H. Park, J. W. Kim, S. S. Lee and J. S. Ha, *ACS Appl. Mater. Interfaces*, 2018, **10**, 28027-28035.
19. C. L. Choong, M.-B. Shim, B.-S. Lee, S. Jeon, D.-S. Ko, T.-H. Kang, J. Bae, S. H. Lee, K.-E. Byun, J. Im, Y. J. Jeong, C. E. Park, J.-J. Park and U. I. Chung, *Adv. Mater.*, 2014, **26**, 3451-3458.
20. L. V. Kayser, M. D. Russell, D. Rodriquez, S. N. Abuhamdieh, C. Dhong, S. Khan, A. N. Stein, J. Ramirez and D. J. Lipomi, *Chem. Mater.*, 2018, **30**, 4459-4468.
21. X. Su, X. Wu, S. Chen, A. M. Nedumaran, M. Stephen, K. Hou, B. Czarny and W. L. Leong, *Adv. Mater.*, 2022, **34**, e2200682.
22. S. Duan, Z. Wang, L. Zhang, J. Liu and C. Li, *ACS Appl. Mater. Interfaces*, 2017, **9**, 30772-30778.
23. K. Huang, M. Chen, G. He, X. Hu, W. He, X. Zhou, Y. Huang and Z. Liu, *Carbon*, 2020, **157**, 466-477.
24. R. Zhou, P. Li, Z. Fan, D. Du and J. Ouyang, *J. Mater. Chem. C*, 2017, **5**, 1544-1551.
25. S. Chung, J. Lee, H. Song, S. Kim, J. Jeong and Y. Hong, *Appl. Phys. Lett.*, 2011, **98**, 153110.

26. S. Jang, C. Kim, J. J. Park, M. L. Jin, S. J. Kim, O. O. Park, T. S. Kim and H. T. Jung, *Small*, 2018, **14**, 1702818.
27. J. Wang, K. Zhang, J. Wang, M. Zhang, Y. Zhou, J. Cheng and D. Kong, *J. Mater. Chem. C*, 2020, **8**, 9440-9448.
28. H. J. Kwon, G. U. Kim, C. Lim, J. K. Kim, S. S. Lee, J. Cho, H. J. Koo, B. J. Kim, K. Char and J. G. Son, *ACS Appl. Mater. Interfaces*, 2023, **15**, 13656-13667.
29. C. A. Silva, J. Lv, L. Yin, I. Jeerapan, G. Innocenzi, F. Soto, Y. G. Ha and J. Wang, *Adv. Funct. Mater.*, 2020, **30**, 2002041.
30. H. W. Liang, Q. F. Guan, Z. Zhu, L. T. Song, H. B. Yao, X. Lei and S. H. Yu, *NPG Asia Mater.*, 2014, **4**, e19.
31. K. H. Kim, M. Vural and M. F. Islam, *Adv. Mater.*, 2011, **23**, 2865-2869.
32. Z. Niu, H. Dong, B. Zhu, J. Li, H. H. Hng, W. Zhou, X. Chen and S. Xie, *Adv. Mater.*, 2013, **25**, 1058-1064.
33. Y.-Y. Lee, H.-Y. Kang, S. H. Gwon, G. M. Choi, S.-M. Lim, J.-Y. Sun and Y.-C. Joo, *Adv. Mater.*, 2016, **28**, 1636-1643.
34. M. Y. Teo, N. Kim, S. Kee, B. S. Kim, G. Kim, S. Hong, S. Jung and K. Lee, *ACS Appl. Mater. Interfaces*, 2017, **9**, 819-826.
35. K. Seyoung, K. Hyunho, S. H. Kumar Paleti, A. El Labban, M. Neophytou, A. H. Emwas, H. N. Alshareef and D. Baran, *Chem. Mater.*, 2019, **31**, 3519-3526.
36. J. E. Hagler, C. Kim, P. Kateb, J. Yeu, N. Gagnon-Lafrenais, E. Gee, S. Audry and F. Cicoira, *Flex. Print. Electron.*, 2022, **7**, 014008.
37. D. H. Kim, H. J. Lee, D. Park, J. H. Yim and H. K. Choi, *Nanoscale*, 2023, **15**, 4620-4627.
38. Y. G. Seol, T. Tran Quang, O.-J. Yoon, I.-Y. Sohn and N.-E. Lee, *J. Mater. Chem.*, 2012, **22**, 23759-23766.
39. E. Bihar, T. Roberts, E. Ismailova, M. Saadaoui, M. Isik, A. Sanchez-Sanchez, D. Mecerreyes, T. Hervé, J. B. De Graaf and G. G. Malliaras, *Adv. Mater. Technol.*, 2017, **2**, 1600251.
40. X. Ma, W. Cai, S. Zhang, J. Guo, X. Peng, Z. Qiu, J. Ying and J. Wang, *New J. Chem.*, 2018, **42**, 692-698.
41. Z. A. Akbar, J.-W. Jeon and S.-Y. Jang, *Energ. Environ. Sci.*, 2020, **13**, 2915-2923.
42. M. Khatib, T. P. Huynh, Y. Deng, Y. D. Horev, W. Saliba, W. Wu and H. Haick, *Small*, 2018, **15**, e1803939.
43. S. Yoon, Y. J. Kim, Y. R. Lee, N.-E. Lee, Y. Won, S. Gandla, S. Kim and H.-K. Kim, *NPG Asia Mater.*, 2021, **13**, 4.
44. S. M. Mehdi, J. Jo, Y. H. Doh, H. W. Dang and K. H. Choi, *J. Polym. Sci. Polym. Phys.*, 2015,

53, 226-233.

45. M. Park, H. J. Kim, I. Jeong, J. Lee, H. Lee, H. J. Son, D.-E. Kim and M. J. Ko, *Adv. Energy Mater.*, 2015, **5**, 1501406.
46. N. M. Nair, J. K. Pakkathillam, K. Kumar, K. Arunachalam, D. Ray and P. Swaminathan, *ACS Appl. Electron. Mater.*, 2020, **2**, 1000-1010.
47. A. Pasha, S. Khasim, A. A. A. Darwish, T. A. Hamdalla, S. A. Al-Ghamdi and S. Alfadhli, *Synth. Met.*, 2022, **283**, 116984.
48. Q. Liu, Z. Xu, W. Qiu, C. Hou, Y. Wang, P. Yao, R. Yu, W. Guo and X. Y. Liu, *RSC Adv.*, 2018, **8**, 18690-18697.
49. I. S. Jin, W. Lee, S. J. Lim, J. H. Ko and J. W. Jung, *Smart Mater. Struct.*, 2020, **29**, 095002.